Examination of surface roughness on light scattering by long ice columns by use of a two-dimensional finite-difference time-domain algorithm

Wenbo Sun, Norman G. Loeb, Gorden Videen, and Qiang Fu

Natural particles such as ice crystals in cirrus clouds generally are not pristine but have additional microroughness on their surfaces. A two-dimensional finite-difference time-domain (FDTD) program with a perfectly matched layer absorbing boundary condition is developed to calculate the effect of surface roughness on light scattering by long ice columns. When we use a spatial cell size of 1/120 incident wavelength for ice circular cylinders with size parameters of 6 and 24 at wavelengths of 0.55 and 10.8 μm, respectively, the errors in the FDTD results in the extinction, scattering, and absorption efficiencies are smaller than ~0.5%. The errors in the FDTD results in the asymmetry factor are smaller than ~0.05%. The errors in the FDTD results in the phase-matrix elements are smaller than ~5%. By adding a pseudorandom change as great as 10% of the radius of a cylinder, we calculate the scattering properties of randomly oriented rough-surfaced ice columns. We conclude that, although the effect of small surface roughness on light scattering is negligible, the scattering phase-matrix elements change significantly for particles with large surface roughness. The roughness on the particle surface can make the conventional phase function smooth. The most significant effect of the surface roughness is the decay of polarization of the scattered light.

OCIS codes: 010.0010, 290.0290, 010.1310, 030.5770, 290.5850, 290.5890.

1. Introduction

Cirrus clouds have an important influence on climate through their effects on radiative transfer. Regularly covering ~20–30% of the globe, cirrus clouds are composed of almost exclusively nonspherical ice crystals of various shapes.[1] Although in theoretical studies and practical applications the ice crystals in cirrus clouds are usually assumed to be smooth-surfaced particles, such as spheres, spheroids, hexagonal columns, circular plates, and bullet rosettes, natural ice crystals in cirrus clouds generally are not pristine but have additional microroughness on their surfaces. In a study for scattering and polarization of light by rough and porous interstellar grains, Perrin and Sivan[2] noted that surface roughness cannot be neglected, in particular in a spectral domain where the grains are not very small compared with the wavelength.

Light scattering by spherical or spheroidal grains with surface or inside defects was also studied by Vaidya and Gupta[3] and Chamaillard and Lafon.[4] They used the discrete dipole approximation[5] for interstellar dust or water–ice particles. The size parameters that they worked on are not larger than ~1.0. Several studies have been conducted for light scattering by deformed spheres.[6–10] However, these studies generally concentrate on the effects of particle-shape irregularity. The conclusions derived from these studies do not necessarily represent those for regular particles with additional microroughness on their surfaces.

The primary limitations in the calculation of light scattering by irregular particles are computer memory and CPU time. Numerical calculation of light scattering by three-dimensional (3-D) particles with surface roughness can be costly or even impractical when particles are larger than the wavelength. In this study we develop a two-dimensional (2-D) finite-difference time-domain[11–16] (FDTD) light-scattering model with a perfectly matched layer[17] (PML), ab-

W. Sun and N. G. Loeb are with the Center for Atmospheric Sciences, Hampton University, Hampton, Virginia 23668. W. Sun can be reached at Mail Stop 420, NASA Langley Research Center, Hampton, Virginia 23681-0001 (e-mail, w.sun@larc.nasa.gov). G. Videen is with the U.S. Army Research Laboratory, Adelphi, Maryland 20783. Q. Fu is with the Department of Atmospheric Sciences, University of Washington, Seattle, Washington 98195.

Received 17 June 2003; revised manuscript received 10 November 2003; accepted 10 December 2003.

0003-6935/04/091957-08$15.00/0

sorbing boundary condition (ABC) to study the effect of surface microroughness on light scattering and absorption by long circular ice columns. In Section 2 the 2-D PML FDTD light-scattering model is introduced. In Section 3 the 2-D PML FDTD model is validated by the analytic method. In Section 4 applications of the 2-D PML FDTD model to long circular ice columns with pseudo-random surface microroughness is presented. Summary and conclusions are in Section 5.

2. Two-Dimensional PML FDTD Light-Scattering Model

In this section we develop a 2-D FDTD program with a PML ABC to calculate the effect of surface roughness on light scattering and absorption by long ice columns. We assume an arbitrarily polarized normal-incident light. In the 2-D FDTD formulations the arbitrarily polarized light can be decomposed into TM and TE components, e.g., the FDTD correspondences of source-free Maxwell's equations for TM polarized light can be written as

$$H_x^{n+1/2}(i, j + 1/2) = H_x^{n-1/2}(i, j + 1/2) - \frac{\Delta t}{\mu(i, j)\Delta s}[E_z^n(i, j + 1) - E_z^n(i, j)], \quad (1a)$$

$$H_y^{n+1/2}(i + 1/2, j) = H_y^{n-1/2}(i + 1/2, j) + \frac{\Delta t}{\mu(i, j)\Delta s}[E_z^n(i + 1, j) - E_z^n(i, j)], \quad (1b)$$

$$E_z^{n+1}(i, j) = \exp\left[-\frac{\varepsilon_i(i, j)}{\varepsilon_r(i, j)}\omega\Delta t\right]E_z^n(i, j) + \exp\left[-\frac{\varepsilon_i(i, j)}{\varepsilon_r(i, j)}\omega\Delta t/2\right] \times \frac{\Delta t}{\varepsilon_r(i, j)\Delta s} \times [H_y^{n+1/2}(i + 1/2, j) - H_y^{n+1/2}(i - 1/2, j) - H_x^{n+1/2}(i, j + 1/2) + H_x^{n+1/2}(i, j - 1/2)], \quad (1c)$$

where H_x, H_y, and E_z denote the magnetic and the electric-field components, respectively; the superscript n denotes the time step; ω is the angular frequency of the light; μ is the local permeability; ε_i and ε_r are the local imaginary and real permittivity, respectively; Δt and Δs are time and space increments, respectively. In this study, to satisfy the Courant–Friedrichs–Levy conditions for the stability of the numerical scheme,[12] we set $\Delta t = 0.5\Delta s/c$, where c denotes the light speed in free space. The accuracy of the FDTD results depends highly on the space increment Δs. In this study, to resolve the small-roughness features on the particle surface, we set

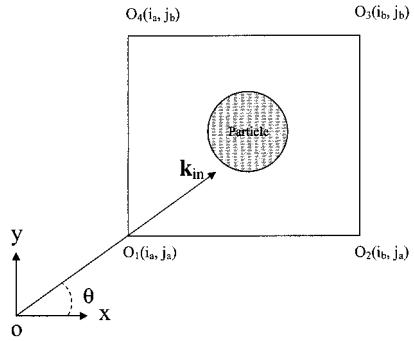

Fig. 1. Geometries of the incident direction and the closed rectangular interface of the total field and the scattered field.

$\Delta s = \lambda/120$ if not specified, where λ is the wavelength in free space.

We use the total- and scattered-field formulation[13–16,18,19] on a closed rectangular curve around the scatterer to implement a plane incident wave in the 2-D FDTD grid. As shown in Fig. 1, e.g., for TM-polarized incident light, the wave source is added to the field components as follows[19]:

At the face $(i = i_a, \ldots, i_b; j = j_a)$,

$$H_x^{n+1/2}(i, j_a - 1/2) = \{H_x^{n+1/2}(i, j_a - 1/2)\}_{(1a)} + \frac{\Delta t}{\mu_0\Delta s}E_{z,\mathrm{inc}}^n(i, j_a), \quad (2a)$$

$$E_z^{n+1}(i, j_a) = \{E_z^{n+1}(i, j_a)\}_{(1c)} - \frac{\Delta t}{\varepsilon_0\Delta s}H_{x,\mathrm{inc}}^{n+1/2}(i, j_a - 1/2). \quad (2b)$$

At the face $(i = i_a, \ldots, i_b; j = j_b)$,

$$H_x^{n+1/2}(i, j_b + 1/2) = \{H_x^{n+1/2}(i, j_b + 1/2)\}_{(1a)} - \frac{\Delta t}{\mu_0\Delta s}E_{z,\mathrm{inc}}^n(i, j_b), \quad (2c)$$

$$E_z^{n+1}(i, j_b) = \{E_z^{n+1}(i, j_b)\}_{(1c)} + \frac{\Delta t}{\varepsilon_0\Delta s}H_{x,\mathrm{inc}}^{n+1/2}(i, j_b + 1/2). \quad (2d)$$

At the face $(i = i_a; j = j_a, \ldots, j_b)$,

$$H_y^{n+1/2}(i_a - 1/2, j) = \{H_y^{n+1/2}(i_a - 1/2, j)\}_{(1b)} - \frac{\Delta t}{\mu_0\Delta s}E_{z,\mathrm{inc}}^n(i_a, j), \quad (2e)$$

$$E_z^{n+1}(i_a, j) = \{E_z^{n+1}(i_a, j)\}_{(1c)} + \frac{\Delta t}{\varepsilon_0\Delta s}H_{y,\mathrm{inc}}^{n+1/2}(i_a - 1/2, j). \quad (2f)$$

At the face ($i = i_b; j = j_a, \ldots, j_b$),

$$H_y^{n+1/2}(i_b + 1/2, j) = \{H_y^{n+1/2}(i_b + 1/2, j)\}_{(1b)} + \frac{\Delta t}{\mu_0 \Delta s} E_{z,\mathrm{inc}}^n(i_b, j), \quad (2g)$$

$$E_z^{n+1}(i_b, j) = \{E_z^{n+1}(i_b, j)\}_{(1c)} - \frac{\Delta t}{\varepsilon_0 \Delta s} H_{y,\mathrm{inc}}^{n+1/2}(i_b + 1/2, j). \quad (2h)$$

Note that, in Eqs. (2), ε_0 and μ_0 are the permittivity and the permeability of free space, respectively; $\{H_x^{n+1/2}(i, j + 1/2)\}_{(1a)}$, $\{H_y^{n+1/2}(i + 1/2, j)\}_{(1b)}$, and $\{E_z^{n+1}(i, j)\}_{(1c)}$ denote the magnetic- and the electric-field components directly from Eqs. (1a)–(1c), respectively. The incident-field components $E_{z,\mathrm{inc}}^n$, $H_{x,\mathrm{inc}}^{n+1/2}$, and $H_{y,\mathrm{inc}}^{n+1/2}$ are from the linear interpolation of the fields produced by an auxiliary one-dimensional FDTD scheme.[19] The incident fields simulated by the one-dimensional FDTD scheme can be decomposed into components in the x, y, and z directions corresponding to the incident angle θ shown in Fig. 1. In practice, calculations of light scattering by randomly oriented (only in the x–y plane for the 2-D case) long columns are realized by varying the incident angle θ in a reasonable increment.

To truncate the computational domain, the 2-D PML ABC developed by Berenger[17] is implemented in the program. The PML creates a nonphysical absorbing layer adjacent to the outer grid boundary with introduction of artificial conductivities and the splitting of electric- or magnetic-field components into subcomponents, e.g., for TM-polarized incidence the electric component E_z is split into two subcomponents E_{zx} and E_{zy}, the field updating equations in the PML can be given as follows[17]:

$$H_x^{n+1/2}(i, j + 1/2) = \exp[-\sigma_y^*(j + 1/2)\Delta t/\mu_0] \times H_x^{n-1/2}(i, j + 1/2) - \frac{\{1 - \exp[-\sigma_y^*(j + 1/2)\Delta t/\mu_0]\}}{\sigma_y^*(j + 1/2)\Delta s} \times [E_z^n(i, j + 1) - E_z^n(i, j)], \quad (3a)$$

$$H_y^{n+1/2}(i + 1/2, j) = \exp[-\sigma_x^*(i + 1/2)\Delta t/\mu_0] H_y^{n-1/2}(i + 1/2, j) + \frac{\{1 - \exp[-\sigma_x^*(i + 1/2)\Delta t/\mu_0]\}}{\sigma_x^*(i + 1/2)\Delta s} \times [E_z^n(i + 1, j) - E_z^n(i, j)], \quad (3b)$$

$$E_{zx}^{n+1}(i, j) = \exp[-\sigma_x(i)\Delta t/\varepsilon_0] E_{zx}^n(i, j) + \frac{\{1 - \exp[-\sigma_x(i)\Delta t/\varepsilon_0]\}}{\sigma_x(i)\Delta s} \times [H_y^{n+1/2}(i + 1/2, j) - H_y^{n+1/2}(i - 1/2, j)], \quad (3c)$$

$$E_{zy}^{n+1}(i, j) = \exp[-\sigma_y(j)\Delta t/\varepsilon_0] E_{zy}^n(i, j) - \frac{\{1 - \exp[-\sigma_y(j)\Delta t/\varepsilon_0]\}}{\sigma_y(j)\Delta s} \times [H_x^{n+1/2}(i, j + 1/2) - H_x^{n+1/2}(i, j - 1/2)], \quad (3d)$$

$$E_z^{n+1}(i, j) = E_{zx}^{n+1}(i, j) + E_{zy}^{n+1}(i, j), \quad (3e)$$

where σ_x and σ_y denote electric conductivities and σ_x^* and σ_y^* denote magnetic conductivities in the x and the y directions, respectively. It is well known that if the electric and magnetic conductivities match, i.e., $\sigma/\varepsilon_0 = \sigma^*/\mu_0$, a plane wave can propagate normally across the interface between the free space and the PML without any reflection. In this study the conductivities are of the form[17]

$$\sigma(\rho) = \sigma_m \left(\frac{\rho}{d}\right)^f, \quad (4)$$

where ρ denotes the grid point position in the PML, d denotes the thickness of the PML, and f is set to 2.5 in this study.[20] The σ_m in Eq. (4) can be derived from a reflection factor:

$$R(0) = \exp\{-[2/(n + 1)](\sigma_m d/\varepsilon_0 c)\}. \quad (5)$$

The reflection factor $R(0)$ is an important user-input parameter. In this study $R(0)$ is set to be 10^{-5} for all the numerical computations.

The incident wave is assumed to be a Gaussian pulse.[12,16] With time-step marching this plane-wave pulse propagates and interacts with the scatterer within the total-field region enclosed by the rectangular curve illustrated in Fig. 1. Outside this total- and scattered-field interface, only scattered fields exist. The near fields in the frequency domain are obtained from the FDTD-produced time series through the discrete Fourier transform at each grid point. The single-scattering properties including the extinction, scattering, and absorption cross sections and the scattering phase functions are calculated by using the near fields in frequency domain.

To calculate the single-scattering properties, we consider a normal slice of the column with unit thickness. For normal incidence there should not be any wave passing through the two sides of the slice. Therefore for this unit-thickness space the volume integral formulations of the single-scattering properties derived in the 3-D FDTD light-scattering models[13,16] can be transformed into 2-D area integral

formulations. The absorption cross section for a slice of the column of unit thickness is

$$\sigma_a = \frac{k}{|E_0|^2} \iint_s \varepsilon_i(\boldsymbol{\xi}) \mathbf{E}(\boldsymbol{\xi}) \cdot \mathbf{E}(\boldsymbol{\xi}) \mathrm{d}^2\xi, \tag{6}$$

where k is the wavenumber and s denotes the area of the column cross section, $\mathbf{E}(\boldsymbol{\xi})$ is the total electric field at a position denoted by vector $\boldsymbol{\xi}$ on the 2-D slice, the asterisk denotes the complex conjugate, and $|E_0|$ is the amplitude of the incident electric field. Note that in Eq. (6), for TM incidence, $|E_0|^2 = |E_{z,\mathrm{inc}}|^2$ and $\mathbf{E} = (0, 0, E_z)$; for TE incidence, $|E_0|^2 = |E_{x,\mathrm{inc}}|^2 + |E_{y,\mathrm{inc}}|^2$ and $\mathbf{E} = (E_x, E_y, 0)$. If the unit incident electric-field amplitude is assumed, the absorption cross sections for TM and TE incidence, respectively, are

$$\sigma_{a,\mathrm{TM}} = k \iint_s \varepsilon_i(\boldsymbol{\xi}) E_z(\boldsymbol{\xi}) E_z^*(\boldsymbol{\xi}) \mathrm{d}^2\xi, \tag{7a}$$

$$\sigma_{a,\mathrm{TE}} = k \iint_s \varepsilon_i(\boldsymbol{\xi}) [E_x(\boldsymbol{\xi}) E_x^*(\boldsymbol{\xi}) + E_y(\boldsymbol{\xi}) E_y^*(\boldsymbol{\xi})] \mathrm{d}^2\xi. \tag{7b}$$

Therefore for unpolarized incident light the absorption cross section per unit length is

$$\sigma_a = \frac{1}{2} (\sigma_{a,\mathrm{TM}} + \sigma_{a,\mathrm{TE}}). \tag{8}$$

The volume integral form of the scattered field in 3-D space[13,16] can also be transformed into 2-D area integral formulations as

$$\mathbf{E}_s(\mathbf{R}) = \iint_s G(\mathbf{R}, \boldsymbol{\xi}) (k^2 \mathbf{II} + \nabla_\xi \nabla_\xi) \cdot (\mathbf{P}/\varepsilon_0) \mathrm{d}^2\xi, \tag{9}$$

where $G(\mathbf{R}, \boldsymbol{\xi})$ is the 2-D Green's function and $\mathbf{II}$ is the unit dyad. The 2-D Green's function can be expressed in a far-field limiting form as[19]

$$G(\mathbf{R}, \boldsymbol{\xi}) = \frac{i^{3/2}}{(8\pi k)^{1/2}} \frac{\exp(ik|\mathbf{R} - \boldsymbol{\xi}|)}{(|\mathbf{R} - \boldsymbol{\xi}|)^{1/2}}. \tag{10}$$

From Eq. (9) the nonzero elements of the amplitude scattering matrix are derived in forms

$$s_1 = \frac{i^{3/2} k^2}{(8\pi k)^{1/2}} \iint_s [1 - \varepsilon(\boldsymbol{\xi})/\varepsilon_0] E_z \exp(-ik\mathbf{r} \cdot \boldsymbol{\xi}) \mathrm{d}^2\xi, \tag{11a}$$

$$s_2 = \frac{i^{3/2} k^2}{(8\pi k)^{1/2}} \iint_s [1 - \varepsilon(\boldsymbol{\xi})/\varepsilon_0] \mathbf{a} \cdot (E_x, E_y) \exp(-ik\mathbf{r} \cdot \boldsymbol{\xi}) \mathrm{d}^2\xi, \tag{11b}$$

where $\mathbf{r}$ denotes the unit vector in the scattering direction and $\mathbf{a}$ denotes the unit vector perpendicular to $\mathbf{r}$ in the scattering plane as shown in Fig. 2. In Eq. (11b) (E_x, E_y) is the electric vector with components E_x and E_y.

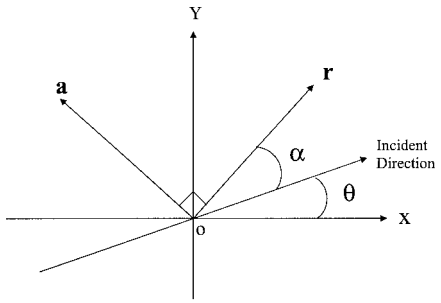

Fig. 2. Geometries of the incident direction, the unit vector in the scattering direction, and the unit vector perpendicular to the scattering direction.

The unpolarized scattering cross section per unit length is from the integral of the scattered intensity around the column, which is

$$\sigma_s = \int_0^{2\pi} \frac{1}{2} (s_1 s_1^* + s_2 s_2^*) \mathrm{d}\alpha, \tag{12}$$

where α is the scattering angle as shown in Fig. 2.

3. Validation of Method

We validate our methodology through a comparison of our numerical results with those obtained from an analytic solution of the scattering from an infinitely long circular cylinder of radius a. Tables 1 and 2 show the single-scattering properties of two circular cylinders with size parameters of 6 and 24, respectively, calculated by the analytic solution and the FDTD method. The refractive index of ice at a wavelength of 0.55 μm ($m = 1.311$) is used in Table 1, and the refractive index of ice at a wavelength of 10.8 μm ($m = 1.4717 + 0.3890i$) is used in Table 2. We see that the FDTD results agree well with the analytic results in both tables. The errors in the FDTD results in the extinction efficiency Q_e, scattering efficiency Q_s, and absorption efficiency Q_a are smaller than ~0.5%. The errors in the FDTD results in asymmetry factor g are smaller than ~0.05%. As an example, Fig. 3 shows a comparison of four independent phase-matrix elements for a circular cylinder with a refractive index of $1.4717 + 0.3890i$ and a size parameter of 24 calculated by the analytic solution and the FDTD method. We can see that the two

Table 1. Single-Scattering Properties of a Cylinder with a Refractive Index of 1.311

	$x = 6$		$x = 24$	
Method	Q_s	g	Q_s	g
Analytic	3.81085	0.91645	2.15320	0.87274
FDTD	3.80545	0.91642	2.15468	0.87423

Table 2. Single-Scattering Properties of a Cylinder with a Refractive Index of 1.4717 + 0.3890*i*

	$x = 6$				$x = 24$			
Method	Q_e	Q_s	Q_a	g	Q_e	Q_s	Q_a	g
Analytic	2.21900	1.11632	1.10268	0.89803	2.10365	1.12070	0.98294	0.91670
FDTD	2.22236	1.11707	1.10529	0.89832	2.10805	1.12276	0.98528	0.91680

results agree well. The errors in the FDTD results in these elements are smaller than ~5%.

4. Application to Particles with Pseudorandom Surface Roughness

The motivation for this research is to study the effect of roughness on ice crystals. Cirrus ice particles often do not resemble pristine hexagonally shaped crystals but often have a roughness due to secondary crystals located on their surfaces. The microroughness associated with cirrus ice crystals is poorly characterized. Our overly simplified model of the surface roughness is to use a normally distributed deviate *rn* with zero mean and unit variance to modify the surface of a cylindrical crystal. A 2-D particle surface can be represented by a radius vector $\mathbf{r}(R, \phi)$, where R denotes the length and ϕ denotes the direction of the radius. In this study we assume that the 2-D particle surface is constructed by a straight-line connection of the ends of 120 radius vectors $\mathbf{r}(R, \phi)$ starting from one origin, as shown in Fig. 4. The length and the direction of each radius vector are pseudorandomly given as

$$R(m) = a[1 + rn(m, s = 1)\sigma], \tag{13a}$$

$$\phi(m) = \frac{m\pi}{60} + rn(m, s = 2)\,\frac{\pi}{180}, \tag{13b}$$

where σ denotes the maximum deviation of the column from a cylinder with a radius of a and s is the seed for the random number series, $m = 0, 1, 2, \ldots, 120$, which is the index number assigned to each individual radius vector. The seed s determines a series of 120 random numbers, and the index number m helps to select an individual number from the series. For this rough-surfaced column we define its size parameter by using the mean radius a, i.e., $x = 2\pi a/\lambda$. The accuracy of the FDTD results is determined by the spatial cell size. To examine whether the spatial cell size used in this study is small enough to resolve the tiny features of the roughness on the column surface, we calculate the light scattering by the column using the FDTD program with different spatial cell sizes. Figure 5 shows the comparison of scattering phase-matrix elements from the rough-surfaced ice column shown in Fig. 4 computed by the FDTD method with spatial cell sizes of $\lambda/60$ and $\lambda/120$, respectively. In these calculations the size parameter of the column is 24 and the refractive index of the column is 1.311. The incident direction is a reverse x direction ($\phi = 0°$). It shows that the results from the FDTD with a spatial cell size of $\lambda/60$ match very well with those from the FDTD with a spatial cell size of $\lambda/120$, which means that the spatial cell size of $\lambda/120$ is good enough for the FDTD simulation of the light scattering by the rough-surfaced column shown in Fig. 4.

A number of numerical simulations are made for randomly oriented 2-D ice columns with a surface microroughness as in Fig. 4. In the FDTD simulations the incident angle varies from 0° to 360° with an increment of 10°. The scattering properties for different incidences are averaged to get the quantities for randomly oriented particles. Figure 6 shows a

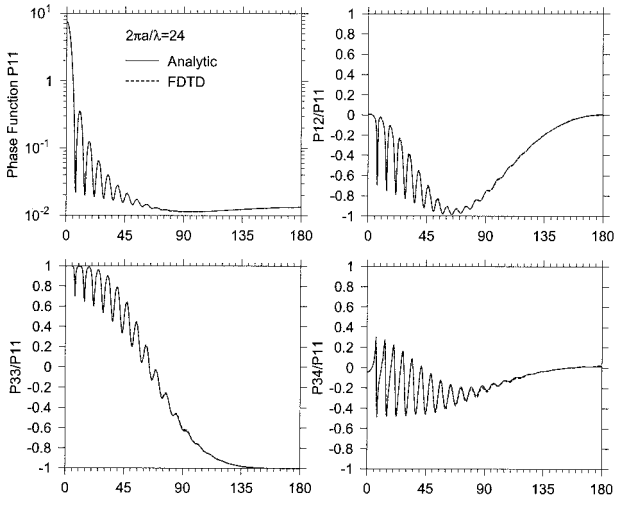

Fig. 3. Comparison of the elements of the scattering phase matrix from analytic and the FDTD solutions for an infinitely long circular cylinder with a refractive index of 1.4717 + 0.3890*i* and a size parameter of 24.

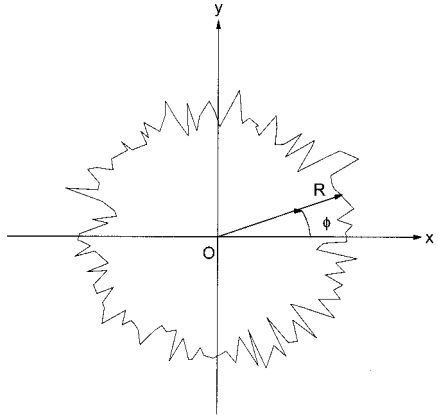

Fig. 4. Cross section of a rough-surfaced column with the maximum deviation from a cylinder, $\sigma = 0.1$.

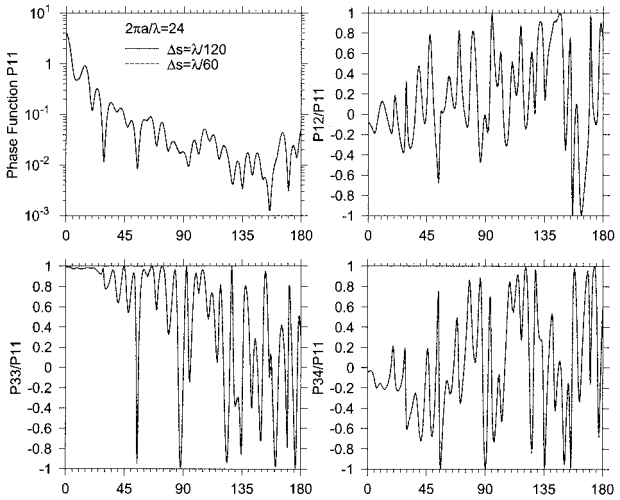

Fig. 5. Comparison of elements of the scattering phase matrix from the rough-surfaced ice column shown in Fig. 4 computed by the FDTD method with spatial cell sizes of $\lambda/60$ and $\lambda/120$, where λ denotes the incident wavelength in free space. The size parameter of the column is 24. The refractive index of the column is 1.311. The incident direction is in the reverse x direction ($\phi = 0°$).

comparison of elements of the scattering phase matrix from a perfect circular cylinder and randomly oriented rough-surfaced ice columns with $\sigma = 0.1$. A refractive index of 1.311 and a size parameter of 6 are used. We can see that the scattering matrix elements change significantly when the particle surface is rough but still retain the general shape of the elements for the perfect-cylinder curves because of the approximately cylindrical shape of the particle. For the larger-size parameter case shown in Fig. 7, where the roughness features are comparable with the incident wavelength, the scattering patterns are strongly affected. The most significant change in the scattering patterns is the decay of the structure in

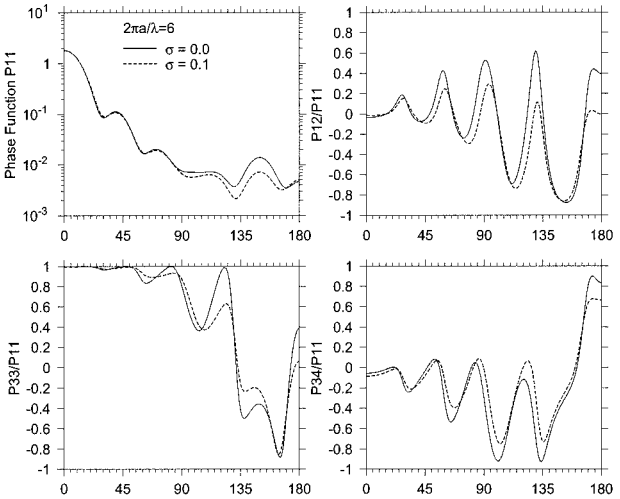

Fig. 6. Comparison of elements of the scattering phase matrix from a perfect circular cylinder and randomly oriented rough-surfaced ice columns with $\sigma = 0.1$. A refractive index of 1.311 and a size parameter of 6 are used.

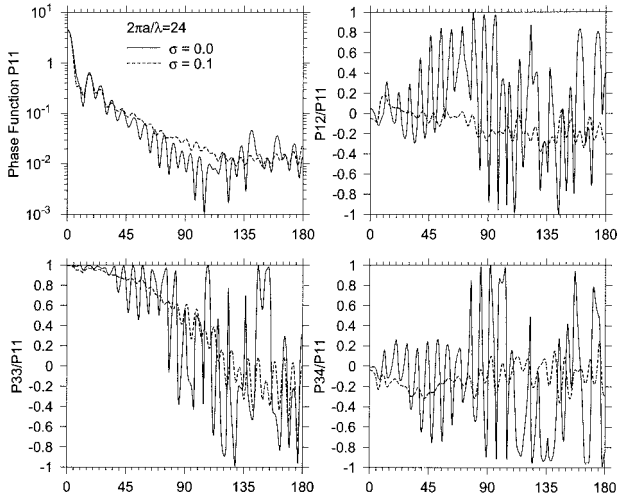

Fig. 7. Same as Fig. 6 but for a size parameter of 24.

the polarization matrix elements with the surface roughness. Except in the forward-scatter region of matrix element P_{33}, the values tend to approach zero; i.e., the light becomes unpolarized. Similar observations of the production of unpolarized light have been measured experimentally from rough[21] and contaminated[22] quartz fibers. From Fig. 7 we can see that the surface roughness of the 2-D particle could be evaluated by using both total and polarized intensity measured at different scattering angles, although further studies are needed to quantify the roughness by using the total and polarized scattering features. As an example, Table 3 shows the relative differences in phase-matrix elements (PME) between the rough-surfaced and the perfect cylinders at a scattering angle of 170° for the case in Fig. 7. We can see that the roughness can cause relative differences in these quantities as large as ~100% at this typical scattering angle.

For strong absorption cases such as using the refractive index of $1.4717 + 0.3890i$, Figs. 8 and 9 show that the effect of surface roughness also alters the scattering signals substantially. However, for both size parameters of 6 and 24 the dependence of the total and the polarized scattered intensity on scattering angle still closely follows that of perfect circular cylinders. The effect of surface roughness on light-

Table 3. Relative Differences in PMEs between the Rough-Surfaced and Perfect Cylinders at a Scattering Angle of 170° for the Case in Fig. 7

	$\left\lvert\frac{\text{PME(rough)} - \text{PME(perfect)}}{\text{PME(perfect)}}\right\rvert \times 100\%$	
PME	$x = 6$ (%)	$x = 24$ (%)
P11	0.4898	32.8340
P12/P11	97.0161	39.0079
P33/P11	6.4548	41.9472
P34/P11	21.5055	109.6298

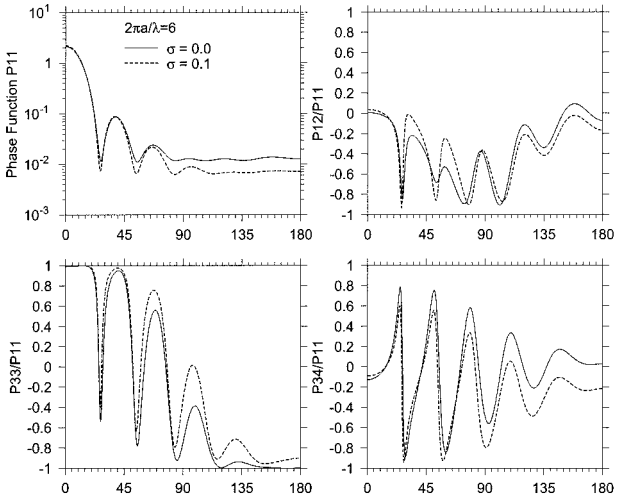

Fig. 8. Comparison of elements of the scattering phase matrix from a perfect circular cylinder and randomly oriented rough-surfaced ice columns with $\sigma = 0.1$. A refractive index of $1.4717 + 0.3890i$ and a size parameter of 6 are used.

scattering quantities in Fig. 9 is different from the nonabsorbing case as shown in Fig. 7.

Although we show the results only for two size parameters, our calculations demonstrate that for size parameters as high as 48, the effect of surface roughness on PME are quite similar. However, compared with the change in particle shape, we found that the effect of roughness on the light scattering is rather small. We tested a smaller roughness ($\sigma = 0.025$) in our study, and the results showed a negligible effect on the scattering properties. In general, to measure the effects of roughness, the roughness must be rather large.

5. Summary and Conclusions

In this study we have developed a 2-D FDTD algorithm with a PML ABC to calculate the effect of surface roughness on light scattering and absorption by long ice columns. When we use a spatial cell size of 1/120 incident wavelength for ice circular cylinders with size parameters of 6 and 24 at wavelengths of 0.55 and 10.8 μm, respectively, the errors in the FDTD results in the extinction, scattering, and absorption efficiencies are smaller than ~0.5%. The errors in the FDTD results in the asymmetry factor are smaller than ~0.5%. The errors in the FDTD results in the PME are smaller than ~5%. By adding a pseudo-random change as large as 10% of the radius of a cylinder, we calculated the scattering properties of randomly oriented rough-surfaced ice columns. We have concluded that, although the effect of small surface roughness on light scattering is negligible, the light-scattering characteristics change significantly for particles with large surface roughness. The roughness of the particle surface can smooth the conventional phase function and can substantially reduce the polarization of the scattered light.

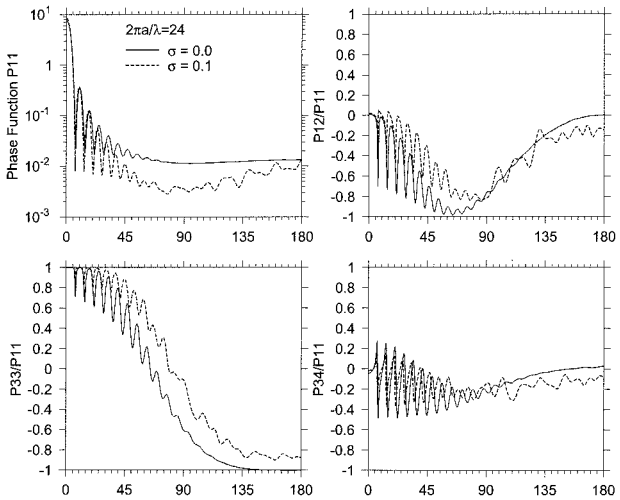

Fig. 9. Same as Fig. 8 but for a size parameter of 24.

This study was supported by NASA's Clouds and the Earth's Radiant Energy System (CERES) grant NAG-1-2318 and NASA grant NAG-1-01096.

References

1. Y. Takano and K. N. Liou, "Radiative transfer in cirrus clouds. Part III: Light scattering by irregular ice crystals," J. Atmos. Sci. **52,** 818–837 (1995).
2. J.-M. Perrin and J.-P. Sivan, "Scattering and polarization of light by rough and porous interstellar grains," Astron. Astrophys. **247,** 497–504 (1991).
3. D. B. Vaidya and R. Gupta, "Extinction by porous silicate and graphite grains," Astron. Astrophys. **328,** 634–640 (1997).
4. K. Chamaillard and J.-P. J. Lafon, "Statistical approach of the effect of roughness on the polarization of light scattered by dust grains," J. Quant. Spectrosc. Radiat. Transfer **70,** 519–528 (2001).
5. E. M. Purcell and C. P. Pennypacker, "Scattering and absorption of light by nonspherical dielectric grains," Astrophys. J. **196,** 705–714 (1973).
6. A. Mugnai and J. J. Wiscombe, "Scattering of radiation by moderately nonspherical particles," J. Atmos. Sci. **37,** 1291–1307 (1980).
7. J. I. Peltoniemi, K. Lumme, K. Muinonen, and W. M. Irvine, "Scattering of light by stochastically rough particles," Appl. Opt. **19,** 4088–4095 (1989).
8. K. Muinonen, T. Nousiainen, P. Fast, K. Lumme, and J. I. Peltoniemi, "Light scattering by Gaussian random particles: ray optics approximation," J. Quant. Spectrosc. Radiat. Transfer **55,** 577–601 (1996).
9. A. Battaglia, K. Muinonen, T. Nousiainen, and J. I. Peltoniemi, "Light scattering by Gaussian particles: Rayleigh-ellipsoid approximation," J. Quant. Spectrosc. Radiat. Transfer **63,** 277–303 (1999).
10. W. Sun, T. Nousiainen, K. Muinonen, Q. Fu, N. G. Loeb, and G. Videen, "Light scattering by Gaussian particles: a solution with finite-difference time-domain technique," J. Quant. Spectrosc. Radiat. Transfer **79-80,** 1083–1090 (2003).
11. K. S. Yee, "Numerical solution of initial boundary value problems involving Maxwell's equation in isotropic media," IEEE Trans. Antennas Propag. **AP-14,** 302–307 (1966).
12. P. Yang and K. N. Liou, "Light scattering by hexagonal ice crystals: comparison of finite-difference time domain and geometric optics models," J. Opt. Soc. Am. A **12,** 162–176 (1995).

13. P. Yang and K. N. Liou, "Finite-difference time-domain method for light scattering by small ice crystals in three-dimensional space," J. Opt. Soc. Am. A **13,** 2072–2085 (1996).
14. W. Sun, Q. Fu, and Z. Z. Chen, "Finite-difference time-domain solution of light scattering by dielectric particles with a perfectly matched layer absorbing boundary condition," Appl. Opt. **38,** 3141–3151 (1999).
15. W. Sun and Q. Fu, "Finite-difference time-domain solution of light scattering by dielectric particles with large complex refractive indices," Appl. Opt. **39,** 5569–5578 (2000).
16. W. Sun, N. G. Loeb, and Q. Fu, "Finite-difference time-domain solution of light scattering and absorption by particles in an absorbing medium," Appl. Opt. **41,** 5728–5743 (2002).
17. J. P. Berenger, "A perfectly matched layer for the absorption of electromagnetic waves," J. Comput. Phys. **114,** 185–200 (1994).
18. D. E. Merewether, R. Fisher, and F. W. Smith, "On implementing a numeric Huygen's source in a finite difference program to illustrate scattering bodies," IEEE Trans. Nucl. Sci. **NS-27,** 1829–1833 (1980).
19. A. Taflove, *Computational Electrodynamics: the Finite-Difference Time Domain Method* (Artech House, Boston, Mass., 1995).
20. G. Lazzi and O. P. Gandhi, "On the optimal design of the PML absorbing boundary condition for the FDTD code," IEEE Trans. Antennas Propag. **45,** 914–916 (1996).
21. G. Videen and W. S. Bickel, "Light-scattering Mueller matrix for a rough fiber," Appl. Opt. **31,** 3488–3492 (1992).
22. G. Videen and W. S. Bickel, "Light-scattering Mueller matrix from a fiber as a function of M_gO contamination," Appl. Opt. **30,** 3880–3885 (1991).